

# MODELING CSR IN A VACUUM CHAMBER BY PARTIAL FOURIER ANALYSIS AND THE DISCONTINUOUS GALERKIN METHOD \*

D. A. Bizzozero<sup>†1</sup>, R. Warnock<sup>2,1</sup>, J. A. Ellison<sup>1</sup>

<sup>1</sup>Department of Mathematics and Statistics, University of New Mexico  
Albuquerque, New Mexico 87131, USA

<sup>2</sup>SLAC National Accelerator Laboratory, Stanford University  
Menlo Park, California 94025, USA

## Abstract

We continue our study [1–3] of CSR from a bunch on an arbitrary curved orbit in a plane. The vacuum chamber has rectangular cross section with possibly varying horizontal width. We make a Fourier transform in  $s - ct$  and use the slowly varying amplitude approximation. We invoke a Fourier expansion in the vertical coordinate  $y$ , which meets the boundary conditions on the top and bottom plates and makes contact with the Bessel equation of the frequency domain treatment. The fields are defined by a PDE in  $s$  and  $x$ , first order in  $s$ , which is discretized in  $x$  by finite differences (FD) or the discontinuous Galerkin method (DG). We compare results of FD and DG, and also compare the computation speeds to our earlier calculations in 3D (paraxial) which did not use the Fourier series in  $y$  [4–8]. This approach provides more transparency in the physical description, and when only a few  $y$ -modes are needed, provides a large reduction in computation time.

## STATEMENT OF THE PROBLEM

### Statement of the Physical Problem

We start with the wave equation for the  $E_y$  and  $H_y$  fields in the Frenet-Serret coordinates  $(s, x, y, t)$ :

$$\nabla^2 E_y - \frac{1}{c^2} \frac{\partial^2 E_y}{\partial t^2} = Z_0 \left( \frac{1}{c} \frac{\partial J_y}{\partial t} + c \frac{\partial \rho}{\partial y} \right), \quad (1a)$$

$$\nabla^2 H_y - \frac{1}{c^2} \frac{\partial^2 H_y}{\partial t^2} = -\frac{R}{x+R} \frac{\partial J_x}{\partial s} + \frac{\partial J_s}{\partial x} + \frac{1}{x+R} J_s. \quad (1b)$$

We shall solve for the fields in a toroidal vacuum chamber with perfectly conducting walls at  $x = x_{in}, x_{out}$  and  $y = \pm h/2$ . The bunch orbit is centered in the chamber and has bending radius  $R$ . We next apply a Fourier transform in  $s - ct$  and a Fourier series in  $y$ . Now the fields and sources are expressed in the form

$$F(s, x, y, t) = \int_{-\infty}^{\infty} dk e^{ik(s-ct)} \sum_{p=1}^{\infty} \phi_p(y) \hat{F}_p(s, x, k), \quad (2)$$

$$\phi_p(y) = \begin{bmatrix} \cos \\ \sin \end{bmatrix} \left( \alpha_p (y + h/2) \right), \quad \alpha_p = \frac{\pi p}{h}.$$

\* Work supported by DOE under DE-FG02-99ER41104 and DE-AC03-76SF00515.

<sup>†</sup> dbizzozze@math.unm.edu

If the vertical distribution of charge is an even function of  $y$ , which we assume, then only odd integers  $p$  are involved. For  $E_y, H_x, H_s, J_y$  the factor  $\phi_p$  contains only cos terms whereas for  $H_y, E_x, E_s, \rho, J_x, J_s$  it contains only sin terms. In the approximation of slowly varying amplitude (paraxial approximation) terms with  $\partial^2/\partial s^2$  are neglected and the transformed equations (1) for  $\hat{F}_p(s, x, k) = \hat{E}_{yp}, \hat{H}_{yp}$  become (with  $\gamma_p^2 = k^2 - \alpha_p^2$ ):

$$\frac{2ikR^2}{(x+R)^2} \frac{\partial \hat{F}_p}{\partial s} = -\frac{\partial^2 \hat{F}_p}{\partial x^2} - \frac{1}{x+R} \frac{\partial \hat{F}_p}{\partial x} - \left( \gamma_p^2 - \frac{(kR)^2}{(x+R)^2} \right) \hat{F}_p + S. \quad (3)$$

For a charge density of the form  $q\lambda(s-ct)H(y)\delta(x)$ , where  $q$  is the charge, the source terms are:

$$S_{\hat{E}} = \sigma \delta(x), \quad S_{\hat{H}} = \tau \left( \delta'(x) + \delta(x)/R \right) \quad (4a)$$

$$\sigma = qZ_0 \alpha_p c \hat{\lambda}(k) H_p, \quad \tau = q\beta c \hat{\lambda}(k) H_p, \quad (4b)$$

where  $\hat{\lambda}$  and  $H_p$  are Fourier transforms of  $\lambda$  and  $H$ . For a Gaussian  $H$  with width  $\sigma_y \ll h$  we have  $H_p = (-1)^{(p-1)/2} (2/h) \exp(-(\alpha_p \sigma_y)^2/2)$ .

The perfectly conducting boundary conditions are guaranteed by:

$$\hat{E}_{yp}|_{x=x_{in}, x_{out}} = 0, \quad \frac{\partial \hat{H}_{yp}}{\partial x}|_{x=x_{in}, x_{out}} = 0. \quad (5)$$

To construct initial conditions for  $\hat{E}_{yp}, \hat{H}_{yp}$ , we assume an infinite straight prior to the entrance of the bend and use the steady-state solutions  $\hat{F}_{p0} = \hat{E}_{yp0}, \hat{H}_{yp0}$  which satisfy:

$$\frac{d^2 \hat{F}_{0p}}{dx^2} - \alpha_p^2 \hat{F}_{0p} = S \quad (6)$$

With the solutions  $\hat{E}_{yp}, \hat{H}_{yp}$  to the initial value problem (3-6) for each  $p$ , we construct the remaining fields through additional relations in Eq. (30), then return to the space-time domain by (2).

### Statement of the Mathematical Problem

To solve (3) numerically, we first introduce a transformation to treat the singularities of (4a):

$$V = \hat{E}_{yp} - \sigma x \Theta(x), \quad (7a)$$

$$W = \hat{H}_{yp} - \tau \Theta(x), \quad (7b)$$

with  $\Theta$  being the Heaviside step function. Under these transformations,  $V, W$  still satisfy (3); however, the sources become:

$$S_V = -\sigma\Theta(x)\left(\frac{1}{x+R} + x\left(\gamma_p^2 - \frac{(kR)^2}{(x+R)^2}\right)\right), \quad (8a)$$

$$S_W = -\tau\Theta(x)\left(\gamma_p^2 - \frac{(kR)^2}{(x+R)^2}\right). \quad (8b)$$

We have eliminated  $\delta$  and  $\delta'$  from the source, gaining a big advantage for the numerical work. A jump in the sources at  $x = 0$  remains, but that too can be removed by a second transformation, which will be described elsewhere.

The boundary conditions for  $V, W$  are:

$$\begin{aligned} V|_{x=x_{in}} &= 0, & V|_{x=x_{out}} &= -\sigma x_{out}, \\ \frac{\partial W}{\partial x}|_{x=x_{in}, x_{out}} &= 0. \end{aligned} \quad (9)$$

Next, we condense (3) to the following for fixed  $k, p$ :

$$i\frac{\partial u}{\partial s} = a(x)\frac{\partial^2 u}{\partial x^2} + b(x)\frac{\partial u}{\partial x} + c(x)u + \tilde{S}_{V,W}(x) \quad (10)$$

with  $u$  representing  $V, W$ , and  $\tilde{S}_{V,W} = (x+R)^2 S_{V,W}/2kR^2$ . It is important to note that our Schrödinger-type equation (10) is only parabolic in the sense of infinite propagation speed. It is hyperbolic-like in the sense that initial conditions are not smoothed by the PDE evolution.

The solutions of (6) to provide initial conditions are found readily by variation of parameters:

$$\begin{aligned} \hat{E}_{yp0}(x) &= -\frac{\sigma}{\alpha_p} \frac{\sinh(\alpha_p x_{out}) \sinh(\alpha_p(x-x_{in}))}{\sinh(\alpha_p(x_{out}-x_{in}))} \\ &+ \frac{\sigma}{\alpha_p} \sinh(\alpha_p x)\Theta(x), \end{aligned} \quad (11a)$$

$$\begin{aligned} \hat{H}_{yp0}(x) &= -\tau \frac{\sinh(\alpha_p x_{out}) \cosh(\alpha_p(x-x_{in}))}{\sinh(\alpha_p(x_{out}-x_{in}))} \\ &+ \tau \cosh(\alpha_p x)\Theta(x). \end{aligned} \quad (11b)$$

## NUMERICAL IMPLEMENTATION

In this section we describe our numerical algorithms for integrating (10) by finite difference (FD) and nodal discontinuous Galerkin (DG) numerical schemes. We use explicit time-stepping in  $s$  for both methods.

### Finite Difference Scheme

We begin by discretization of  $[x_{in}, x_{out}]$  into  $N_{res} + 1$  equidistant nodes spaced by  $\Delta x$ . The nodal coordinates are defined by  $x_i = x_{in} + (i-1)\Delta x$  and  $u_i = u(x_i)$ . We define the 4th order differentiation operators by:

$$\begin{aligned} \frac{du}{dx}\Big|_{x_i} &\approx \frac{u_{i-2} - 8u_{i-1} + 8u_{i+1} - u_{i+2}}{12\Delta x}, \\ \frac{d^2u}{dx^2}\Big|_{x_i} &\approx \frac{-u_{i-2} + 16u_{i-1} - 30u_i + 16u_{i+1} - u_{i+2}}{12\Delta x^2}. \end{aligned} \quad (12)$$

For points near the boundaries, i.e.  $i = 1, 2, N_{res}, N_{res} + 1$ , we use lopsided 5 point stencils. For explicit time stepping, we employ a leap-frog scheme. It is important to note: the leap-frog scheme is unstable for the heat equation [9] but stable for our Schrödinger-type equation in (10). The leap-frog scheme is:

$$u^{n+1} = u^{n-1} + 2\Delta s \Phi(u^n) \quad (13)$$

with  $\Phi(u^n)$  denoting the right-hand-side of (10) with the discretizations (12) at  $s = n\Delta s$ . For stability, we take:

$$\Delta s = C_{CFL} k \Delta x^2. \quad (14)$$

In our tests,  $C_{CFL} < 0.3$  results in a stable scheme for  $p \lesssim 40$ . Due to the oscillatory nature of the solution for large  $p$ , a smaller CFL constant must be taken if larger  $p$ -modes are desired.

The boundary conditions on  $V$  are imposed by setting  $V_1 = 0$  and  $V_{N_{res}+1} = -\sigma_p x_{out}$  while the boundary conditions for  $W$  are imposed with a one-sided derivative stencil and solving for  $W_1$  and  $W_{N_{res}+1}$  as functions of  $W_{2,\dots,5}$  and  $W_{N_{res}-3,\dots,N_{res}}$  respectively. The initial conditions on  $V, W$  are computed analytically from (11).

### Discontinuous Galerkin Scheme

We derive our DG scheme in some detail since it is not as well known as FD. DG methods have features taken from finite element (FE) and finite volume methods (FV). Solutions are represented by polynomials local to each element as in FE; however, the PDE can be represented in an explicit semi-discrete form. The PDE is satisfied using fluxes between elements similar to FV. This results in a scheme which can maintain high-order accuracy ( $hp$ -adaptivity) and stability for wave-dominated problems [10].

We rewrite the PDE in (10) in first order form as

$$i\frac{\partial u}{\partial s} = a(x)\frac{\partial q}{\partial x} + b(x)q + c(x)u + f, \quad q = \frac{\partial u}{\partial x}. \quad (15)$$

To find an approximate solution, we begin by partitioning the domain  $[x_{in}, x_{out}]$  into  $K$  elements of polynomial degree  $N$ . The total number of nodes is given by  $(N+1)K$ . We next focus on a particular element  $k$  (note, this  $k$  is *not* related to Fourier transform in (2)). We approximate the solution on this element in the Lagrange polynomial basis:

$$u^k(x, s) = \sum_{j=1}^{N+1} u_j^k(s) \ell_j^k(x), \quad (16)$$

$$q^k(x, s) = \sum_{j=1}^{N+1} q_j^k(s) \ell_j^k(x), \quad (17)$$

with  $\ell_j^k(x_i^k) = \delta_{ij}$  for nodal coordinates  $x_i^k$ . The derivatives of  $u$  in (15) are given by differentiating (16). The terms  $f$ ,  $cu$  and  $bq$  are replaced by their natural interpolating poly-

mials

$$(cu)^k = \sum_{j=1}^{N+1} c_j^k u_j^k(s) \ell_j^k(x), \quad (bq)^k = \sum_{j=1}^{N+1} b_j^k q_j^k(s) \ell_j^k(x), \quad (18)$$

$$f^k = \sum_{j=1}^{N+1} f_j^k(s) \ell_j^k(x)$$

and  $a \partial_x q$  is replaced by

$$a^k \sum_{j=1}^{N+1} q_j^k(s) [\ell_j^k(x)]', \quad (19)$$

where  $a^k$  is the value of  $a$  at the midpoint of element  $k$ . Note that each of these is a polynomial of degree  $N$  (or less). Equation (19) assumes  $a$  does not vary much on element  $k$ , which is certainly true in our case, however, we are investigating alternatives which do not make such an assumption. Inserting (16), (18), (19) into (15) we obtain the following residuals  $\mathcal{R}_{1,2}^k(x, s)$  defined by

$$\mathcal{R}_1^k(x, s) = i \frac{\partial u^k}{\partial s} - a^k \frac{\partial q^k}{\partial x} - (bq)^k - (cu)^k - f^k, \quad (20a)$$

$$\mathcal{R}_2^k(x, s) = q^k - \frac{\partial u^k}{\partial x}. \quad (20b)$$

We now require that the residuals  $\mathcal{R}_{1,2}^k(x, s)$  be approximately orthogonal to the  $\ell_i^k$ . This yields  $N+1$  equations for each  $(u_j^k, q_j^k)$  of the form

$$\int_{\mathcal{D}^k} \mathcal{R}_1^k(x, s) \ell_i^k(x) dx \approx 0, \quad \int_{\mathcal{D}^k} \mathcal{R}_2^k(x, s) \ell_i^k(x) dx \approx 0, \quad (21)$$

for  $i = 1, \dots, N+1$ . Clearly, requiring these to be zero will not yield a viable algorithm, as there would be no coupling between elements. The heart of DG is to couple adjacent elements using the so-called flux condition. This is obtained by integrating the  $[\ell_i^k(x)]'$  terms by parts, inserting the flux condition, and then reversing the integration by parts. We illustrate this on  $\mathcal{R}_2^k(x, s)$ .

$$\begin{aligned} \int_{\mathcal{D}^k} -\frac{\partial u^k}{\partial x} \ell_i^k dx &= \int_{\mathcal{D}^k} u^k \ell_i^k(x)' dx - [u^k \ell_i^k]_{x_1^k}^{x_{N+1}^k} \approx \\ \int_{\mathcal{D}^k} u^k \ell_i^k(x)' dx - [u^{k*} \ell_i^k]_{x_1^k}^{x_{N+1}^k} &= \\ \int_{\mathcal{D}^k} -\frac{\partial u^k}{\partial x} \ell_i^k dx + [u^k - u^{k*}] \ell_i^k & \Big|_{x_1^k}^{x_{N+1}^k} \end{aligned} \quad (22)$$

but the calculation is identical for the  $x$ -derivative of  $q$  in (21). The approximation step introduces  $u^*$  (and  $q^*$ ) which give rise to the numerical fluxes which combine boundary information from the two elements in contact at the interface at  $x_1^k$  or  $x_{N+1}^k$ . While many choices of numerical fluxes exist, we opt to use a local DG flux [10] of the form:

$$\begin{aligned} u^*(x_1^k) &= u_1^k, & u^*(x_{N+1}^k) &= u_{N+1}^{k+1}, \\ q^*(x_1^k) &= q_{N+1}^{k-1}, & q^*(x_{N+1}^k) &= q_{N+1}^k. \end{aligned} \quad (23)$$

The motivation for these fluxes is to model an upwind scheme as was done for parabolic equations and obtain an optimal order of convergence (see p.247-253 in [10]).

We define the vectors  $\ell^k(x) = (\ell_1^k(x), \dots, \ell_{N+1}^k(x))^T$  and similarly for  $\mathbf{u}^k(s)$  and  $\mathbf{q}^k(s)$ . We also introduce the mass and stiffness matrices

$$\mathcal{M}_{ij}^k = \int_{x_1^k}^{x_{N+1}^k} \ell_i^k \ell_j^k dx, \quad \mathcal{S}_{ij}^k = \int_{x_1^k}^{x_{N+1}^k} \frac{d\ell_i^k}{dx} \ell_j^k dx. \quad (24)$$

Thus (21) and (22) yield:

$$\mathbf{q}^k = (\mathcal{M}^k)^{-1} \mathcal{S}^k \mathbf{u}^k - (\mathcal{M}^k)^{-1} [(u - u^*) \ell^k]_{x_1^k}^{x_{N+1}^k}, \quad (25a)$$

$$\begin{aligned} i \frac{d\mathbf{u}^k}{ds} &= a^k (\mathcal{M}^k)^{-1} \mathcal{S}^k \mathbf{q}^k - a^k (\mathcal{M}^k)^{-1} [(q - q^*) \ell^k]_{x_1^k}^{x_{N+1}^k} \\ &+ \mathcal{B}^k \mathbf{q}^k + \mathcal{C}^k \mathbf{u}^k + \mathbf{f}^k. \end{aligned} \quad (25b)$$

Here  $\mathcal{B}^k = \text{diag}(b_1^k, \dots, b_{N+1}^k)$  and similarly for  $\mathcal{C}^k$ .

In the code we combine all  $K$  elements, thus we can arrange the solution as an  $(N+1) \times K$  array with mass and stiffness matrices common to all elements. This approach enables the right-hand-side operations to be done using dense matrix-matrix multiplication. Boundary conditions are handled by adjustment of the fluxes (23). Dirichlet conditions such as for  $V$  are imposed by:

$$\begin{aligned} u^*(x_1^1) &= u(x_{in}), & u^*(x_{N+1}^K) &= u(x_{out}), \\ q^*(x_1^1) &= q_1^1, & q^*(x_{N+1}^K) &= q_{N+1}^K, \end{aligned} \quad (26)$$

and Neumann conditions such as for  $W$  are imposed on  $q^*$  instead of  $u^*$ . The  $(\mathbf{u}, \mathbf{q})$  systems for  $V$  and  $W$  are evolved in  $s$  separately using a Runge-Kutta scheme. The restriction for  $\Delta s$  scales as in (14) with  $\Delta x$  as the minimal distance between two nodes on an element. We use Legendre-Gauss-Lobatto quadrature nodes (see p.43-51 in [10]) due to advantages in matrix conditioning; however, this choice of nodes imposes severe restrictions on  $\Delta s$  at high orders  $N$ . A balance of  $K$  and  $N$  is needed for optimal efficiency.

## NUMERICAL RESULTS

In this section we examine several aspects for a line charge model (i.e.  $\sigma_y \rightarrow 0$ ). First we compare results for  $V$  in the FD and DG schemes of the previous section, emphasizing both computational accuracy and efficiency. Next, we examine the convergence of the Fourier series sum over  $p$  of  $\hat{E}_{yp}$ . Lastly, we compute the longitudinal impedance from a relation for  $\hat{E}_{sp}$  using  $V$  and  $W$ .

### Finite Difference versus Discontinuous Galerkin

For our numerical tests, we use the following parameters (as in [3, 6, 8]):

$$\begin{array}{l|l} x_{in} & = -0.030 \text{ m} & x_{out} & = 0.030 \text{ m} \\ h & = 0.020 \text{ m} & R & = 1.000 \text{ m} \\ q & = 10^{-12} \text{ C} & \beta & = 1 \\ k & = 8 \cdot 10^3 \text{ m}^{-1} & p & = 1 \end{array}$$

A common grid of points in  $x$  is used for the error comparisons of both FD and DG methods. A reference solution for  $V$  at  $s = 0.200$  m is computed by the FD scheme with  $N_{res} = 5760$ . The FD scheme errors are tabulated below.

$N_{res}$	240	480	960	1920
$L^\infty$ Error	1.46e-4	1.06e-5	1.31e-6	4.58e-7
$L^2$ Error	1.24e-4	9.08e-6	1.40e-6	4.61e-7
Time	0.4 s	2.4 s	6.9 s	15.0 s

Our FD method exhibits almost optimal self-convergence (convergence with respect to a higher resolution solution), but tapers off at higher resolutions. We attribute this to the jump discontinuities at  $x = 0$  of the source terms in (10).

Next, the DG scheme with the same parameters is compared for varying order  $N$  and elements  $K$ . A reference solution for  $V$  is computed using  $(N, K) = (12, 80)$  which is compared on the set of nodes for  $(N, K) = (2, 20)$ , common to all solutions.

$K \setminus N$	2	4	6	8
20	2.91e-2 0.04 s	9.01e-3 0.22 s	5.67e-4 1.0 s	1.97e-5 2.8 s
40	8.89e-3 0.10 s	1.92e-4 1.0 s	2.18e-6 4.4 s	3.36e-8 14 s
80	1.88e-3 0.50 s	1.22e-5 5.0 s	3.64e-8 24 s	1.82e-9 77 s

Above, we list the  $L^\infty$  (top),  $L^2$  (middle), and CPU times (bottom) for varying values of  $K$  and  $N$ . In both the FD and DG methods, the order of self-convergence becomes sub-optimal once the resolution is high enough. Again, this loss of self-convergence is attributed to the discontinuous sources as in FD. Both FD and DG methods display comparable efficiency by comparing the CPU times in the tables for similar errors.

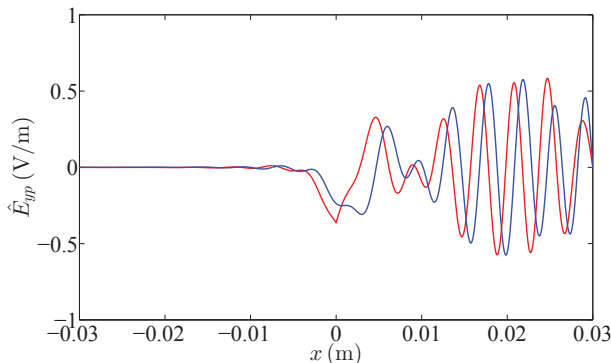


Figure 1: Real (red) and imaginary (blue) parts of DG reference solution for  $\hat{E}_{yp}$  using  $N = 12$ ,  $K = 80$ ,  $p = 1$ ,  $k = 8 \cdot 10^3 \text{ m}^{-1}$ , at  $s = 0.200$  m.

## Fourier Series Convergence

To construct the solutions in  $y$  we use the Fourier series as defined in (2). We concentrate on  $\hat{E}_y$  defined as:

$$\hat{E}_y = \sum_{p=1}^{\infty} \hat{E}_{yp} \cos(\alpha_p(y + h/2)) \quad (27)$$

It is important to note that while each  $\hat{E}_{yp}$  is bounded, the infinite sum introduces a singularity at  $(x, y) = (0, 0)$  for a line charge model. We wish to study the  $L^2$  self-convergence of the partial sums in (27). Thus we subtract the singularity adopting the approach used in [4–8]. The singular term in  $\hat{E}_y$ , by the expression in [4], is:

$$\hat{E}_y^b = \frac{qZ_0c\hat{\lambda}(k)}{2\pi} \frac{y}{x^2 + y^2}. \quad (28)$$

Defining  $\hat{E}_y^r = \hat{E}_y - \hat{E}_y^b$ , we obtain

$$\hat{E}_y^r = \sum_{p=1}^{\infty} [\hat{E}_{yp} - \hat{E}_{yp}^b] \cos(\alpha_p(y + h/2)), \quad (29)$$

with  $\hat{E}_{yp}^b$  as the Fourier series components of (28). Thus, we can examine the  $L^2$  self-convergence of  $\hat{E}_y^r$ . We take the  $p_{max} = 39$  partial sum ( $p = 1, 3, \dots, p_{max}$ ) as a reference solution for (29) for  $k = 8 \cdot 10^3 \text{ m}^{-1}$ . This solution is compared to the partial sums for varying  $p_{max}$ .

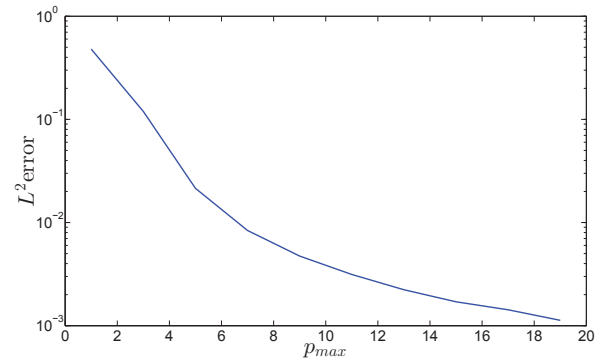


Figure 2:  $L^2$  error  $\hat{E}_y^r$  for varying  $p_{max}$ , with  $1441 \times 481$   $(x, y)$  grid,  $k = 8 \cdot 10^3 \text{ m}^{-1}$ , and  $s = 0.200$  m.

The self-convergence plot in Figure 2 shows only a few  $p$ -modes are necessary to obtain a solution accurate to  $10^{-2}$ . The solutions were computed in  $\sim 100$  seconds for  $p_{max} = 19$  at this resolution. In contrast, in [3], this took  $\sim 1000$  seconds for the same parameters using a 2D FD method. Thus, this 1D approach provides a large computational speed-up over the 2D FD method in [3] using the same computer hardware. The reference solution of  $\hat{E}_y^r$  as a surface plot is displayed in Figure 3.

## CSR Impedance

In this section we compute the longitudinal impedance by examining the dependence of  $\hat{E}_s$  on  $kR$ . The  $\hat{E}_s$  field Fourier

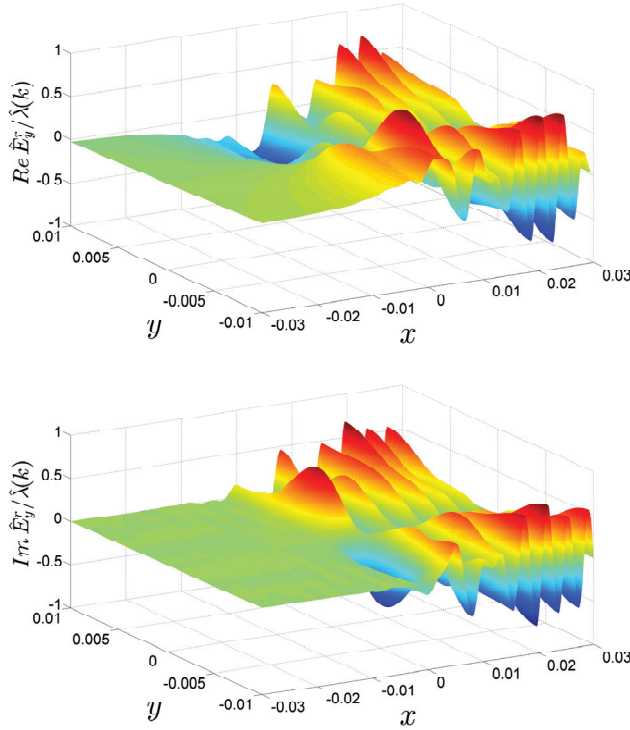


Figure 3: Reference solution for  $Re[\hat{E}_y^r]/\hat{\lambda}(k)$  (top),  $Im[\hat{E}_y^r]/\hat{\lambda}(k)$  (bottom) with  $p_{max} = 39$ ,  $1441 \times 481$  ( $x, y$ ) grid,  $k = 8 \cdot 10^3 \text{ m}^{-1}$ , and  $s = 0.200 \text{ m}$ .

series components are given in terms of the  $p$ -dependent  $V$  and  $W$  by:

$$\hat{E}_{sp} = \frac{-1}{\gamma_p^2} \left[ \frac{\alpha_p R}{x+R} \left( ik(V + \sigma x \Theta) + \frac{\partial V}{\partial s} \right) - ik Z_0 \frac{\partial W}{\partial x} \right]. \quad (30)$$

We mention here that the transforms in  $s - ct$  and  $y$  also yield formulas for  $\hat{E}_{xp}$ ,  $\hat{H}_{xp}$ ,  $\hat{H}_{sp}$  which depend only on  $V$  and  $W$  and their  $s$  and  $x$  derivatives. The  $\partial/\partial s$  terms in (30) are computed by the right-hand-sides of (10). Also of note, the imaginary part of the function  $\hat{E}_{sp}$  becomes very sharply peaked at  $x = 0$  with increasing  $p$  and thus requires finer spatial resolution as the desired accuracy is increased. Numerical experiments suggest that the values of  $\hat{E}_s$  are inaccurate for  $x \in \{-\Delta x, 0, \Delta x\}$  and that  $\hat{E}_s$  is smooth. Thus, we fit a spline to the points  $x \in \{-3\Delta x, -2\Delta x, 2\Delta x, 3\Delta x\}$  and use this in the associated interval. For this numerical test we use the following parameters:

$$\begin{array}{l|l} x_{in} = -0.032 \text{ m} & x_{out} = 0.078 \text{ m} \\ h = 0.032 \text{ m} & R = 7.143 \text{ m} \\ q = 10^{-12} \text{ C} & \beta = 1 \end{array}$$

We examine the value of  $\hat{E}_s$  at  $(x, y) = (0, 0)$  at the end of the bend at  $s = 2.00 \text{ m}$ . This solution for  $\hat{E}_s$  is computed using  $N_{res} = 480$  and  $p_{max} = 9$  with the spline correction. The result is shown in Figure 4, where we see a smooth solution with no visual numerical artifacts.

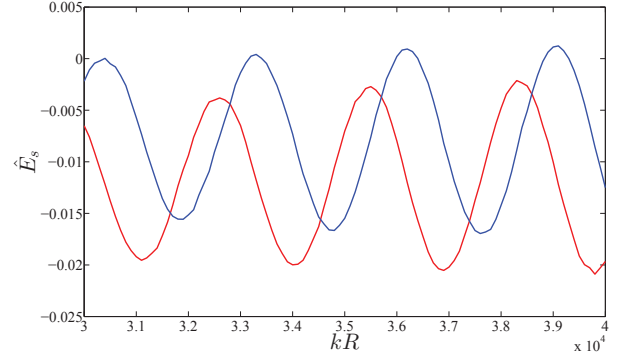


Figure 4: Above,  $Re[\hat{E}_s]$  (red),  $Im[\hat{E}_s]$  (blue) is plotted versus  $kR$  evaluated at  $(x, y) = (0, 0)$  using  $p_{max} = 9$  modes with  $\hat{\lambda}(k)$  set to  $1/(2\pi)$ .

## CONCLUSION

### Summary

We have modeled CSR in a rectangular toroidal bend and achieved results similar to [3] in a fraction of the computation time. Our new method revolving around the Fourier series in  $y$  has greatly reduced the computational complexity of the system and resulted in reasonable approximations to the CSR fields using only a few  $p$ -modes.

The comparison between FD and DG methods enabled us to explore newer numerical techniques and make decisions on future codes based on the different methods. We have shown DG to be superior in the full 2D problem without the Fourier series in  $y$  [3].

### Future Work

We aim to adjust our algorithms to allow for perturbations in the wall positions  $x_{in}(s)$  and  $x_{out}(s)$  to more accurately describe complex vacuum chambers. This adjustment must be made carefully as to not violate the paraxial approximation. We have currently developed an approach using a coordinate transformation to a constant-width chamber but need to examine computational limitations (particularly for complex chamber geometries with large excursions).

Another area of interest is in dropping the paraxial approximation to examine the fields in a chamber with arbitrary walls. Our ongoing analysis suggests the use of a time-domain (non-paraxial) approach to treat Maxwell's equations in that setting.

## ACKNOWLEDGMENTS

We would like to thank the following people for their support on this project: Stephen Lau and Daniel Appelö for valuable insights on numerical algorithms, and Jack Bergstrom for valuable questions and discussions.

## REFERENCES

- [1] G. Bassi, J. A. Ellison, K. Heinemann, R. Warnock, "Microbunching Instability in a Chicane: Two-Dimensional

- Mean Field Treatment”, *Phys. Rev. ST Accel. Beams* **12**, 080704 (2009).
- [2] K. Heinemann, D. Bizzozero, J. A. Ellison, S. R. Lau, G. Bassi, “Rapid integration over history in self-consistent 2D CSR modeling”, Proceedings of ICAP2012, Rostock-Warnemunde, Germany, August 2012. See [jacow.org](http://jacow.org) for the paper and slides at TUSDC2, i.e., <http://accelconf.web.cern.ch/AccelConf/ICAP2012/papers/tusdc2.pdf>
- [3] D. Bizzozero, J. A. Ellison, K. A. Heinemann, S. R. Lau, “Paraxial Approximation in CSR Modeling Using the Discontinuous Galerkin Method”, Proceedings of FEL13, New York, August 2013. See [jacow.org](http://jacow.org) for the paper at MOPSO06, i.e., <http://accelconf.web.cern.ch/AccelConf/FEL2013/papers/mopso06.pdf>
- [4] T. Agoh and K. Yokoya, “Calculation of coherent synchrotron radiation using mesh”, *Phys. Rev. ST Accel. Beams* **7**, 054403 (2004).
- [5] G.V. Stupakov and I.A. Kotelnikov, “Calculation of coherent synchrotron radiation impedance using the mode expansion method”, *Phys. Rev. ST Accel. Beams* **12**, 104401 (2009).
- [6] D. Zhou, K. Ohmi, K. Oide, L. Zang, and G. Stupakov, “Calculation of Coherent Synchrotron Radiation Impedance for a Beam Moving in a Curved Trajectory”, *Jpn. J. Appl. Phys.* **51**, 016401 (2012).
- [7] T. Agoh, *Dynamics of Coherent Synchrotron Radiation by Paraxial Approximation*, Ph.D. Dissertation, University of Tokyo, December (2004).
- [8] D. Zhou, *Coherent Synchrotron Radiation and Microwave Instability in Electron Storage Rings*, Ph.D. Dissertation, The Graduate University for Advanced Studies, September (2011).
- [9] J. Strikwerda, *Finite Difference Schemes and Partial Differential Equations* (Pacific Grove, CA: Wadsworth & Brooks/Cole Advanced Books & Software, 1989).
- [10] J. Hesthaven and T. Warburton, *Nodal Discontinuous Galerkin Methods* (New York: Springer, 2008).